Self-similar picosecond pulse compression for supercontinuum generation at mid-infrared wavelength in silicon strip waveguides

Yujun Cheng [a], Jinhui Yuan [a,b,*], Chao Mei [a], Feng Li [b,*], Zhe Kang [b], Binbin Yan [a], Xian Zhou [c], Qiang Wu [d], Kuiru Wang [a], Xinzhu Sang [a], Keping Long [c], Chongxiu Yu [a], and Gerald Farrell [e]

[a] State Key Laboratory of Information Photonics and Optical Communications, Beijing University of Posts and Telecommunications, Beijing, China
[b] Photonics Research Centre, Department of Electronic and Information Engineering, The Hong Kong Polytechnic University, Hong Kong, China
[c] Department of Computer and Communication Engineering, University of Science and Technology Beijing, Beijing, China
[d] Department of Physics and Electrical Engineering, Northumbria University, Newcastle upon Tyne, United Kingdom
[e] Photonics Research Centre, Dublin Institute of Technology, Dublin, Ireland
**Corresponding authors: yuanjinhui81@bupt.edu.cn, enlf@polyu.edu.hk*

Abstract: Self-similar pulse compression has important application in highly coherent supercontinuum (SC) generation. In this paper, we numerically present the mid-infrared self-similar picosecond pulse compression in a tapered suspended silicon strip waveguide, which is designed with exponentially decreasing dispersion profile along the direction of propagation. When the variation of the Kerr nonlinear coefficient $\gamma(z)$, linear and nonlinear losses, higher-order nonlinearity, and higher-order dispersion are taken into consideration, the simulation result shows that a 1 ps input pulse centred at wavelength 2.8 μm could be self-similarly compressed to 47.06 fs in a 3.9-cm waveguide taper, along with a compression factor F_c of 21.25, quality factor Q_c of 0.78, and negligible pedestal. After that, the compressed pulse is launched into a uniform silicon strip waveguide, which is used for the generation of SC. We numerically demonstrate that the coherence of the generated SC by the compressed pulse can be significantly improved when compared to that generated directly by the picosecond pulse. The simulation results can be used to realize on-chip mid-infrared femtosecond light source and highly coherent supercontinuum, which can promote the development of on-chip nonlinear optics.
Keywords: self-similar pulse compression; silicon strip waveguide; supercontinuum generation

1. Introduction

Recently, silicon-based mid-infrared nonlinear photonics has acquired a lot of attentions because of the advancement in light sources and passive components in the mid-infrared spectral region [1–5]. One of the crucial nonlinear phenomena is the supercontinuum (SC) generation in the mid-infrared region, which is crucial for applications such as molecular detection [6], nonlinear spectroscopy [7], optical frequency comb generation [8], etc. In SC generation, the pulse duration is a deterministic parameter that affects the coherence and bandwidth of the SC obtained. Highly coherent SC can typically be obtained with ultrashort pulses shorter than 100 fs [9]. When longer pulses are used as pump for SC generation in the anomalous dispersion region of nonlinear media, the coherence of the generated SC is seriously degraded because the SC is generated by modulation instability (MI) and disordered soliton fissions [10,11]. Thus, it is necessary to use shorter pump to generate the highly coherent mid-infrared SC. However, the generation of such femtosecond pulse sources in mid-infrared region remains a challenge. Mid-infrared pulses can be obtained by nonlinear processes such as optical frequency down-conversion based on difference frequency generation, optical parametric oscillator or optical parametric amplification [12]. But nonlinear processes require high power ultrashort pulse pump sources, which are bulky and sensitive to the environment. Furthermore, it is hard to have the phase matching condition satisfied over the broad spectra of femtosecond pulses. Semiconductor sources such as quantum cascade lasers and lead-salt diodes can be also employed for mid-IR pulse generation [12]. However, they in general cannot generate short duration pulses. Thus, generation of femtosecond pulses and highly coherent mid-infrared SC directly with picosecond pump pulses is highly desirable.

Several nonlinear pulse compression schemes have been proposed to obtain ultrashort pulses from much longer pulses [13–18]. Among them, self-similar pulse compression can realize large compression factors without generation of pedestal in the short nonlinear media. Self-similar pulse compression has already been demonstrated numerically in step index fiber, photonic crystal fiber (PCF), and silicon waveguide tapers with appropriately designed dispersion or nonlinearity varying profiles [18–20]. For silica optical fibers and PCFs, the required peak powers of the initial pulses reach kilowatt class, and fiber taper a few meters long are difficult to fabricate. In contrast, silicon waveguides have much stronger Kerr nonlinearity. Thus, it is possible to achieve self-similar pulse compression with waveguides only a few centimeters long for input pulses with peak power less than one Watt. Moreover, since silicon waveguides are CMOS compatible, it is easy to control the waveguide dimension in fabrication. Silicon waveguides have been utilized in many applications [21]. A combination of a silicon waveguide and high-Q microresonator can be used as a sensitive sensor to detect minute changes in refractive index based on evanescent waves [22] and frequency comb based optical clock [23]. On-chip ultrashort pulse sources in silicon waveguide have also attracted much interest because of their extensive applications in integrated all-optical signal process systems and nonlinear spectroscopy. In 2010, Colman et al. demonstrated the compression of a 3-ps pulse to 580 fs in a small-footprint photonics crystal waveguide [24]. In the same year, Tan et al. reported a chip-scale pulse compressor on silicon which achieved the compression factor of 7 for the 7-ps input pulse [25]. In 2016, we theoretically demonstrated the compression of a 1 ps pulse centred at wavelength 1.55 μm to 81.5 fs in a 6-cm long As_2S_3-Si slot tapered waveguide, but two-photon absorption (TPA) and higher-order dispersion limited further compression [19]. On-chip self-similar pulse compression in the mid-infrared spectral region in 2017 was demonstrated preliminarily in a silicon ridge waveguide taper [20]. But the SC generation pumped by such compressed pulses was not discussed.

In this paper, a tapered suspended silicon strip waveguide with an exponentially decreasing dispersion profile along the direction of propagation is designed. We demonstrate the mid-infrared self-similar picosecond pulse compression in the designed waveguide taper. The compressed pulse is then injected into a section of uniform silicon strip waveguide to generate highly coherent SC. This paper is organized as follows. In Section 2, the generalized nonlinear Schrödinger equation (GNLSE) and theory of self-similar pulse compression in tapered silicon waveguide are given. Section 3 presents a tapered suspended silicon strip waveguide for the self-similar picosecond pulse compression. In Section 4, the mid-infrared self-similar pulse compression in the designed tapered waveguide is numerically investigated. In Section 5, the generation of highly coherent SC is investigated using the compressed pump pulse. Conclusions are drawn in Section 6.

2. Theoretical model

Considering the loss, second and higher-order dispersion (HOD), variation of the Kerr nonlinear coefficient $\gamma(z)$, and higher-order nonlinearity (HON), the propagation dynamics of optical signals in waveguide can be described by a GNLSE [26,27] given by

$$\frac{\partial A}{\partial z}+\frac{\alpha_0 A}{2}-\sum_{m\geq 2}^{6} i^{m+1}\frac{\beta_m(z)}{m!}\frac{\partial^m A}{\partial t^m}=i\gamma(z)(1+i\tau_s\frac{\partial}{\partial t})|A|^2 A-\frac{\gamma_{3PA}}{3A_{eff}^2(z)}|A|^4 A, \tag{1}$$

where $A(z, t)$ is the slowly varying envelope of the electric field, z is the propagation distance, and t is the retarded time. α_0 represents the linear loss. $\beta_m(z)$ (m represents the integers from 2 to 6) are the m-th order dispersion coefficient of the waveguide at z. The self-steepening effect is measured by $\tau_s = 1/\omega_0$, where ω_0 is the angular frequency of the optical carrier. $\gamma(z)$ and $A_{eff}(z)$ are respectively the Kerr nonlinear coefficient and the effective mode area at z, which are defined as [28]

$$A_{eff}=\frac{\left(\iint_{-\infty}^{+\infty}|F(x,y)|^2\,dxdy\right)^2}{\iint_{-\infty}^{+\infty}|F(x,y)|^4\,dxdy}\quad\text{and}\quad \gamma=\frac{\omega n_2(x,y)}{cA_{eff}}, \tag{2}$$

where $F(x, y)$ and $n_2(x, y)$ correspond to the transverse distributions of the optical field and the nonlinear-index coefficient. In the mid-infrared range of 2.2 to 3.2 μm, including the pump wavelength 2.8 μm, TPA is negligible and the three-photon absorption with coefficient γ_{3PA} will dominate the nonlinear loss in the propagation [29–31].

When $\alpha_0 = 0$, $\beta_m(z) = 0$ if $m\neq 2$, $\tau_s = 0$, and TPA = 0, the remaining parameters varying nonlinear Schrödinger equation (NLSE)

$$i\frac{\partial A}{\partial z}-\frac{\beta_2(z)}{2}\frac{\partial^2 A}{\partial t^2}+\gamma(z)|A|^2 A=0 \tag{3}$$

can support self-similar pulse compression [32,33]. When the variation of the Kerr nonlinear coefficient $\gamma(z)$ is a constant and the 2nd dispersion coefficient decreases exponentially as $\beta_2(z)=\beta_2(0)e^{-\sigma z}$ along z, where $\sigma=\beta_2(0)\xi > 0$, $\beta_2(0)$ is the 2nd dispersion coefficient at $z = 0$ and ξ is the chirp factor of the initial pulse, Eq. (3) is rewritten as

$$i\frac{\partial A}{\partial z}-\frac{\beta_2(0)e^{-\beta_2(0)\xi z}}{2}\frac{\partial^2 A}{\partial t^2}+\gamma_0|A|^2 A=0. \tag{4}$$

From [19], during the propagation the pulse width $T(z)$ and peak power $P(z)$ will evolve as

$$T(z)=T_0e^{-\sigma z}\quad\text{and}\quad P(z)=P_0e^{\sigma z}, \tag{5}$$

where T_0 is the width of initial pulse and P_0 is the peak power of initial pulse. From Eq. (5), the pulse width T and peak power P decreases and increases exponentially along the propagation z, respectively. The pulse compression factor F_c, which is defined as the ratio of full width at half maximum (FWHM) of the input pulse to that of the output pulse, depends on the value of σz. For hyperbolic secant pulse, FWHM=1.767T_0, σz is related to the ratio of $\beta_2(z)$ to $\beta_2(0)$, so it is crucial to design an appropriate waveguide taper to obtain a large value of F_c in self-similar pulse compression.

3. Design of tapered silicon strip waveguide

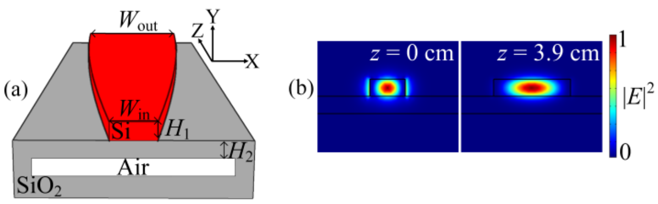

Fig. 1. (a) Sketch of the tapered suspended silicon strip waveguide. (b) The mode field distributions of the quasi-TE at the wavelength of 2.8 μm at the input port (z = 0 cm) and output port (z = 3.9 cm), respectively.

We design a tapered suspended silicon strip waveguide, as shown in Fig. 1(a). Compared to the traditional strip waveguide, the suspended structure can reduce the absorption loss in the silica substrate and achieve well-confined mode field distribution. In practice, the designed waveguide taper can be fabricated by a combination of plasma enhanced chemical vapor deposition and silicon deep etching technologies [34–36]. In Fig. 1(a), the waveguide widths W_{in} and W_{out} at the input and output ports are 0.82 and 1.77 μm, respectively. The waveguide height H_1 is 0.39 μm and the membrane height H_2 is 0.4 μm. Fig. 1(b) shows the mode field distribution of the fundamental quasi-TE at the input and output ports calculated at a wavelength of 2.8 μm.

The 2nd dispersion coefficient β_2 and nonlinear coefficient γ of the fundamental quasi-TE mode at different waveguide widths are calculated by the finite element method. For self-similar pulse compression, a larger variation range of β_2 will achieve a larger compression factor. However, the value of β_2 should not be too small to avoid HODs [37,38]. Fig. 2(a) shows the curves of β_2 calculated for different waveguide widths. From Fig. 2(a), the value of β_2 decreases gradually as the waveguide width varies from

0.82 to 1.77 μm at the wavelength 2.8 μm. In order to achieve the exponentially decreasing dispersion profile along z, the waveguide taper profile is accordingly designed as shown in Fig. 2(b). At the wavelength of 2.8 μm, β_2 and γ are calculated as functions of the propagation z, as shown in Fig. 2(c). From Fig. 2(c), β_2 decreases exponentially from −9.32 to −0.248 ps^2/m along the direction of increasing z. In contrast, the variation of γ is not monotonic. γ first increases from the initial value of 17.37 W^{-1}/m to the maximum 19.20 W^{-1}/m and then decreases from 19.20 to 13.66 W^{-1}/m when z increases from 0.6 to 3.9 cm. Because the relative variation of γ is much smaller than that of β_2, it is reasonable to consider γ a constant and the variation a perturbation during the propagation process. The tiny geometric variations do not affect the values β_2 and γ significantly. As a result, the influence of the fabrication tolerance on the pulse compression is small.

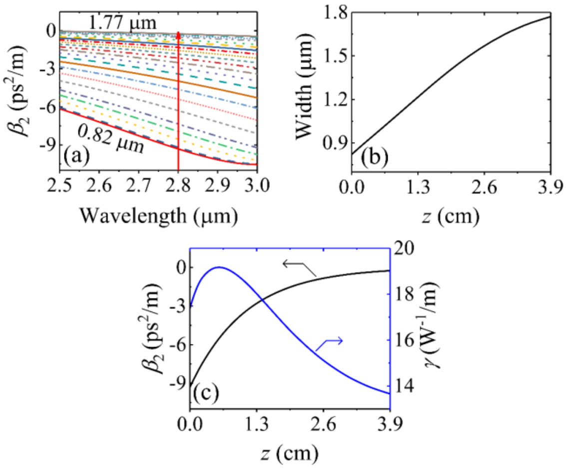

Fig. 2. (a) The 2nd dispersion coefficient β_2 of quasi-TE mode for different waveguide widths from 0.82 to 1.77 μm, (b) waveguide width profile along z, and (c) β_2 (left axis) and nonlinearity coefficient γ (right axis) as functions of z.

4. Mid-infrared self-similar pulse compression

To investigate the self-similar pulse compression in the tapered silicon strip waveguide, we use the Runge-Kutta method to solve Eq. (4) and model the pulse propagation dynamics when γ maintains constant and β_2 decreases exponentially. The constant nonlinear coefficient is calculated as the effective value

$$\gamma_{eff} = \frac{1}{L}\int_0^L \gamma(z)dz, \tag{6}$$

where $\gamma(z)$ is given in Fig. 2(c). For the waveguide taper, γ_{eff} = 16.48 W^{-1}/m. A hyperbolic secant pulse at wavelength of 2.8 μm with a FWHM of 1 ps is injected into the waveguide taper. To maintain the fundamental soliton, the peak power of the initial pulse is set as 1.76 W. The initial chirp ξ is −9.97 ps^{-2}. Fig. 3 shows the evolutions of the temporal and normalized spectral profiles for the ideal case without considering the HOD, HON, linear and 3PA-induced nonlinear losses, and variation of $\gamma(z)$. From Fig. 3, the pulse is gradually compressed in the temporal domain and broadened in the spectral domain. During the propagation, the pulse profile is well maintained. The width of pulse is compressed from 1 ps to 26.61 fs, along with F_c = 37.58. The peak power of pulse is increased from 1.76 to 65.92 W. We use the compression quality factor Q_c, which is defined as $Q_c = P_{out}/(P_{in}F_c)$, to evaluate the pulse compression performance [16,39]. For the ideal case, Q_c is 1. During the pulse compression, the temporal and spectral profiles of the pulse are both symmetrical without pedestal.

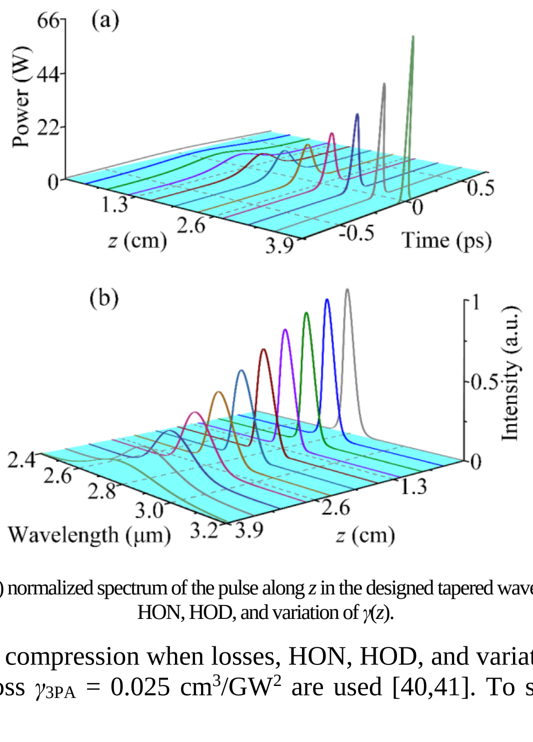

Fig. 3. The dynamics of (a) temporal waveform and (b) normalized spectrum of the pulse along z in the designed tapered waveguide for the ideal case without considering the losses, HON, HOD, and variation of $\gamma(z)$.

Next, we study the self-similar pulse compression when losses, HON, HOD, and variation of $\gamma(z)$ are all considered. The linear loss α_0 = 0.026 dB/cm and nonlinear loss γ_{3PA} = 0.025 cm^3/GW^2 are used [40,41]. To satisfy the condition of the fundamental soliton, the peak power of initial pulse is decreased to 1.67 W since the nonlinear coefficient $\gamma(z=0)$ is 17.37 W^{-1}/m, which is larger than $\gamma_{\rm eff}$. Fig. 4 shows the evolutions of the temporal and normalized spectral profiles, respectively. From Fig. 4, the pulse is compressed from 1 ps to 47.06 fs, and the peak power is increased from 1.67 to 27.63 W. F_c and Q_c are 21.25 and 0.78, respectively. Compared with the ideal case, both F_c and Q_c are decreased, which indicates that the self-similar compression process is perturbed. Moreover, the spectral profile becomes asymmetric during the propagation.

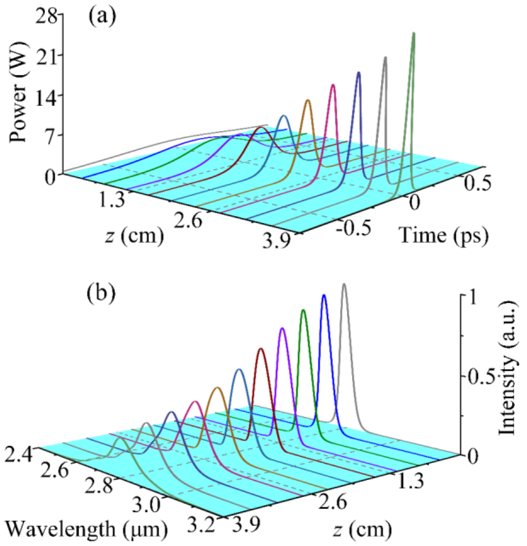

Fig. 4. The dynamics of (a) temporal waveform and (b) normalized spectrum of the pulse along z in the designed tapered waveguide when the losses, HON, HOD, and variation of $\gamma(z)$ are considered.

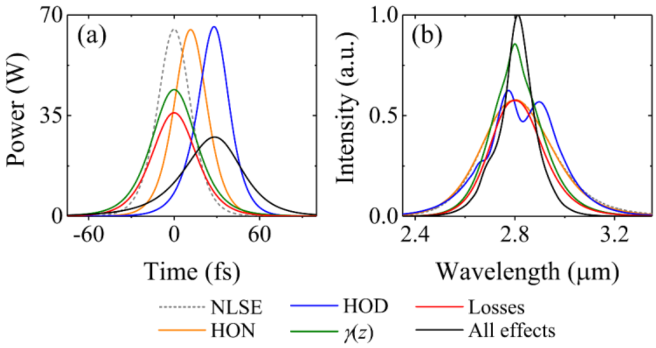

Fig. 5. (a) Temporal and (b) normalized spectra profiles of the output pulses when the HON (orange curves), HOD (blue curves), variation of $\gamma(z)$ (olive curves), and losses including α_0 and 3PA-induced loss (red curves) are considered, respectively. The ideal (NLSE, gray dashed curves) and realistic (All effects, black curves) cases of the output pulses are also given.

In the following, we will investigate the influence of each effect through comparing the pulse propagation when the effects are considered separately. Fig. 5 shows the temporal waveforms and normalized output spectra of the output pulses when the losses, HOD, HON, and variation of $\gamma(z)$ are separately considered. The ideal (NLSE) and realistic (All effects) cases are also given for comparison. The corresponding values of FWHM, peak power, and compression factor F_c for different cases are shown in Table 1. From Fig. 5 and Table 1, the HON and HOD delay the temporal waveform by 12 fs and 28 fs, respectively, while the peak power of the output waveforms changed only a little. In contrast, the $\gamma(z)$ and losses reduce the peak power of the output waveforms significantly. Moreover, both the HOD and $\gamma(z)$ introduce distortions to the output spectra. Although the perturbative effects have diverged the propagation from the ideal case, picosecond pulse is still well compressed.

Table 1 The values of the FWHM, peak power and F_c of the output pulse under different cases

Cases	NLSE	HON	HOD	$\gamma(z)$	Losses	All effects
FWHM (fs)	26.61	26.83	25.39	36.78	36.14	47.06
Power (W)	65.92	65.64	66.83	44.33	36.25	27.63
F_c	37.58	37.27	39.38	27.18	27.67	21.25

Although the HOD has minor impact on the temporal waveform, it deforms the output spectrum. To quantify the impact of HOD, the different-order dispersion lengths L_{Dm} (m represents the integers from 2 to 6) are plotted in Fig. 6(a), where L_{Dm} is calculated as

$$L_{Dm} = T_0^m(z) \big/ \left|\beta_m(z)\right|, \tag{7}$$

where $T_0(z)$ and $\beta_m(z)$ are the pulse width and m-th order dispersion coefficient at z, respectively. The ratio L_{D2}/L_{D3} is also plotted to evaluate the relative contribution of 3rd dispersion. From Fig. 6(a), L_{D2} and L_{D3} decrease monotonically as the optical spectrum of the pulse increases during the propagation. For L_{D2}/L_{D3} shown in Fig. 6(b), the maximum value is less than 0.55, which indicates that $\beta_3(z)$ has a weak influence on the self-similar pulse propagation. In addition, the values of L_{D4}, L_{D5}, and L_{D6} are much larger than L_{D2}, so the influences of $\beta_4(z)$, $\beta_5(z)$, and $\beta_6(z)$ are much weaker than $\beta_2(z)$.

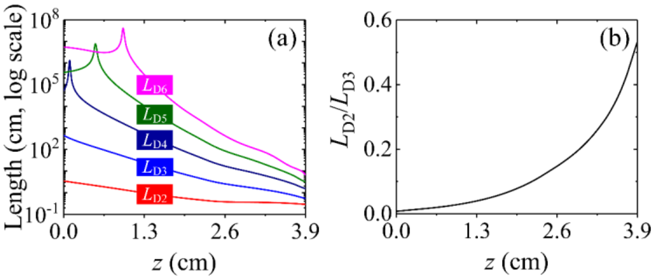

Fig. 6. (a) The variations of different-order dispersion lengths L_{D2} (red curve), L_{D3} (blue curve), L_{D4} (dark blue curve), L_{D5} (olive curve), and L_{D6} (magenta curve). (b) The value profiles of L_{D2}/L_{D3} change along *z*.

The evolutions of the FWHM and peak power of the pulse during the self-similar compression are shown in Fig. 7, respectively, when different effects are considered. From Fig. 7, the FWHM and peak power curves overlap well with that of the ideal case in the range of $z < 2.3$ cm. After $z = 2.3$ cm, the curves of the HON, HOD, $\gamma(z)$, losses, and all effects are gradually deviated from the ideal case. Especially for the cases with $\gamma(z)$, losses, and all effects, the deviations grow quickly along the propagation. Clearly, the simultaneous decreasing of $\gamma(z)$ and the peak power jointly decrease the nonlinear effect, which is hence unable to balance the dispersion to maintain the fundamental soliton condition. Thus, the self-similar propagation condition cannot be satisfied, and the quality of pulse compression is degraded.

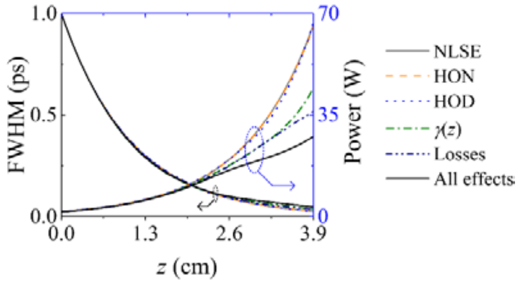

Fig. 7. The variations of FWHM (left axis) and (b) peak power (right axis) of the pulse along *z* within the tapered waveguide when considering HON (orange dashed curves), HOD (blue dotted curves), variation of $\gamma(z)$ (olive dash-dotted curves), and losses including α_0 and 3PA-induced loss (dark blue dash-dot-dotted curves), respectively. The ideal (NLSE, gray solid curves) and realistic (All effects, black solid curves) cases are also plotted.

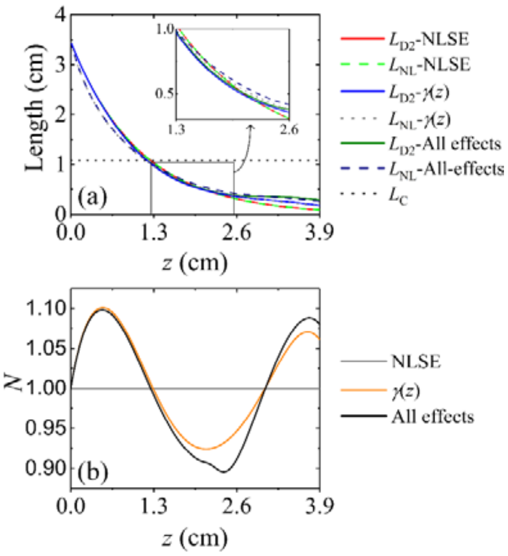

Fig. 8. (a) The dynamics of the 2nd dispersion length L_{D2} and nonlinear length L_{NL} along *z* in the tapered waveguide when the $\gamma(z)$, and all effects are considered. The ideal case and chirp length L_C are also plotted for comparison, and the detail profiles ranged from 1.3 cm to 2.6 cm are shown in the inset. (b) The variations of soliton number *N* along *z* for these three corresponding different cases.

In the ideal case of self-similar pulse compression described by Eq. (4), the fundamental soliton condition should be maintained during the whole propagation, i.e. $L_{D2}(z)=L_{NL}(z)$, where $L_{NL}(z)=1/[\gamma(z)P_0(z)]$ represents the nonlinear length. When the two curves of L_{D2} and L_{NL} are plotted together, the separation between them will evidently indicate the deviation of the propagation from the ideal case. The variations of L_{D2} and L_{NL} along *z* in the waveguide taper are shown in Fig. 8(a) when the $\gamma(z)$, ideal case, and all effects are respectively considered. The chirp length $L_C=1/\sigma$ is also included to evaluate the contribution of the linear part and nonlinear part to the self-similar pulse compression [42]. From Fig. 8(a), $L_{D2}=L_{NL}$ can be satisfied at all *z* values for the ideal case. In Fig. 8(a), for variation of $\gamma(z)$, L_{NL} is smaller than L_{D2} when $z<1.2$ cm, which means that the effect of nonlinearity is stronger than the dispersion. It should be noted that both L_{D2} and L_{NL} are larger than L_C in this region, which means dechirping, i.e. the linear part is the dominant effect to compress the pulse. When 1.2 cm$<z<$2.3 cm, L_{NL} is larger than L_{D2}, which indicates that the effect of nonlinearity is weaker than the dispersion. In this region, L_{D2} and L_{NL} are smaller than L_C, thus the nonlinear part dominates the pulse compression. At the output port of the tapered waveguide, L_{NL} is nearly equal to L_{D2}. When all effects are considered, similar trends but bigger deviations are viewed for L_{D2} and L_{NL}. The corresponding soliton number $N^2 = L_{D2}/L_{NL}$ are also plotted in Fig. 8(b). According to Fig. 8, the fundamental soliton is maintained during the pulse compression.

The self-similar pulse compression can be achieved in the designed waveguide taper without inclusion of the random noise has been demonstrated in the above results. In practice, the random noise is unavoidable. An input pulse with random noise can be described as [9]

$$A(t)=\sqrt{P_0}\,\mathrm{sech}(\frac{t}{T_0})\left[e^{i\xi t^2/2}+\eta\hat{N}e^{i2\pi\hat{U}}\right], \tag{8}$$

where η is the relative magnitude of the random noise. $\hat{N}$ is a variable which satisfies the standard normal distribution with standard deviation 1 and mean 0. $\hat{U}$ is a uniformly distributed variable, whose value is between 0 and 1. When η is set as 0.05, the input and compressed output pulses are shown in Fig. 9, respectively. The compressed output pulse without random noise (η = 0) is also plotted in Fig. 9(b) for comparison. From Fig. 9, the 1 ps input pulse with many burrs can still be self-similarly compressed to 47.06 fs, while the random noise is significantly suppressed during the compression process.

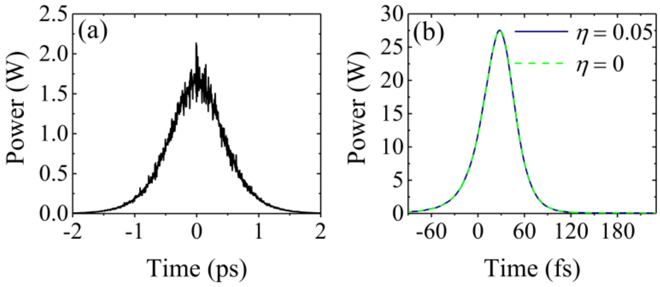

Fig. 9. (a) The 1 ps initial pulse with random noise (black solid curve), and (b) the self-similarly compressed output pulse with (dark blue solid curve) and without (green dash curve) the random noise.

In summary, the mid-infrared self-similar picosecond pulse compression in the tapered waveguide has been demonstrated. A 1 ps pulse can be compressed to 47.06 fs in a 3.9-cm long propagation. Besides, the process of pulse compression is insensitive to the random noise of the initial pulse. The compressed pulse with high quality is expected to demonstrate a good performance in SC generation.

5. Compressed pulse for the SC generation

Usually, a highly coherent SC can be easily obtained by using all-normal dispersion media pumped by the picosecond or femtosecond pulses. To compare the coherence of the SC generated with the compressed and uncompressed pump pulses, an uniform suspended silicon strip waveguide with an anomalous dispersion profile between the two zero-dispersion wavelengths is designed to generate the SC. Fig. 10(a) shows the three-dimensional schematic diagram of the waveguide. The heights h_1, h_2, and width w are 0.3, 1.8, and 1.43 μm, respectively. Fig. 10(b) and the inset show the calculated β_2 curve of the quasi-TE mode and its mode profile at wavelength 2.8 μm. From Fig. 10(b), two zero-dispersion wavelengths are located at 2.75 and 3.42 μm, respectively. The value of γ is 15.17 W^{-1}/m at 2.8 μm.

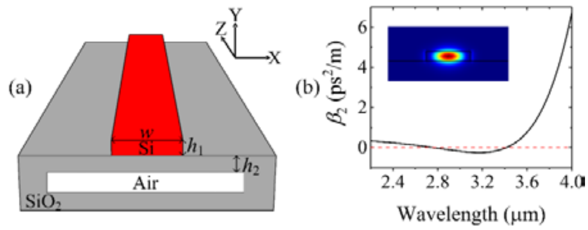

Fig. 10. (a) The three-dimensional schematic diagram of the uniform silicon strip waveguide designed. (b) The 2nd dispersion coefficient β_2 of the quasi-TE mode, and the inset shows the quasi-TE mode profile calculated at wavelength 2.8 μm.

Table 2 Taylor-series expansion coefficients of the dispersion

β_2	□-3.51×10^{-2} ps²/m	β_7	-5.36×10^{-10} ps⁷/m
β_3	3.29×10^{-3} ps³/m	β_8	1.12×10^{-11} ps⁸/m
β_4	□-1.04×10^{-5} ps⁴/m	β_9	-3.14×10^{-13} ps⁹/m
β_5	□-4.05×10^{-7} ps⁵/m	β_{10}	1.78×10^{-14} ps¹⁰/m
β_6	1.84×10^{-8} ps⁶/m		

We launch the initial 1 ps pulse with peak power of 1.67 W and the compressed 47.06 fs pulse with peak power of 27.63 W into the silicon waveguide, respectively. The corresponding soliton number N are 26.9 for the 1 ps pulse and 5.1 for the 47.06 fs pulse. A sufficient coupling is assumed for the injection of the compressed pulse into the uniform silicon strip waveguide based on the adiabatic optical coupling method [43,44]. The evolutions of spectra and temporal profiles during the propagation in the strip waveguide of the two different pump pulses are shown in Fig. 11, respectively. In our simulation, the propagation loss of the silicon strip waveguide is the same as the realistic case in Section 4, and the HOD is calculated up to 10th order, as shown in Table 2. In Fig. 11, the top and bottom figures show the output and input spectra and temporal waveforms, respectively. The middle figures show the spectral and temporal evolutions of the input pulse along propagation. When the pump pulse is launched in anomalous dispersion region, SC generation should be a combination of a series of nonlinear effects, including self-phase modulation (SPM), MI, self-steepening, soliton fission, dispersive wave (DW) generation, and cross-phase modulation (XPM) between the DW and solitons [45–50]. When a long pump pulse is adopted, MI will lead the SC generation into a random process, which can be observed in the region of z>400 mm of the middle-left evolutions with the 1 ps pump. In contrast, the SC generation process is smooth and clean with the 47.06 fs pulse, where soliton fission rather than MI is the dominant effect to expand the spectrum. As a result, the SC generated with the 1 ps pump spans from 2.43 to 3.13 μm at −40 dB level, which is narrower than that that with the 47.06 fs pulse, which spans from 2.13 to 4.03 μm. Clearly, the higher peak power of the 47.06 fs pulse has enhanced the SPM and XPM effects during the SC generation. Moreover, the red-shifted DW can be generated at longer wavelength which is clearly shown at ~3.9 μm. In addition, the waveguide length required for the 1 ps pulse is 700 mm, which is much longer than the 12 mm length required for the 47.06 fs pulse. By comparing the top figures of Figs. 11(a) and 11(b), the coherence of the SC generated with the compressed 47.06 fs pulse is greatly improved since MI is effectively suppressed.

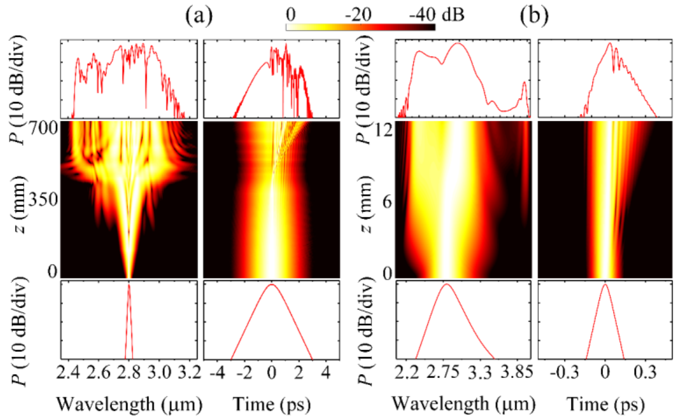

Fig. 11. The evolutions of spectral and temporal profiles along z of (a) the 1 ps pulse, and (b) the compressed 47.06 fs pulse at $\eta = 0.01$. The top and bottom figures show the spectral and temporal profiles of pulse at the output and input ports of the waveguide, respectively.

Benefiting from the suppression of the MI process, the SC spectrum obtained with the 47.06 fs pump pulse is smoother and should be more deterministic, which implies a higher coherence than that with the 1 ps pump pulse. In order to compare the coherence of the SC generated with the 1 ps and 47.06 fs pulses, the first-order coherence $g_{12}^{(1)}$ of the output spectra is calculated as [28,51]

$$\left|g_{12}^{(1)}(\lambda)\right| = \left|\frac{\langle \tilde{\psi}_1^*(\lambda)\tilde{\psi}_2(\lambda)\rangle}{\sqrt{\langle|\tilde{\psi}_1(\lambda)|^2\rangle\langle|\tilde{\psi}_2(\lambda)|^2\rangle}}\right|, \tag{9}$$

where $\tilde{\psi}(\lambda)$ is the spectrum of SC under investigation. The angular brackets denote the ensemble average over the independent pairs of spectra generated from 50 shot-to-shot simulations with random noise.

When the 1 ps pulse with peak power of 1.67 W is used, the output spectra and $g_{12}^{(1)}$ of the SC are shown in Figs. 12(a) and 12(c), respectively. The spectra of the 50 shots with η = 0.01 are represented by the overlapped orange plots in Fig. 12(a) with a dashed curve to plot the averaged spectrum, where the spectral deviations of the 50 shots are clearly observed. All values of $g_{12}^{(1)}$ are less than 0.83 in the whole spectral range as shown in Fig. 12(c). In contrast, with the compressed pump pulse, the variations of SC spectra are almost negligible in most range as shown in Fig. 12(b), and the value of $g_{12}^{(1)}$ shown in Fig. 12(d) is very close to 1 within the wavelength range from 2.3 to 4.0 μm. By comparing Figs. 12(c) and 12(d), the coherence of SC has been significantly enhanced by using the compressed pulse to replace the picosecond pump pulse.

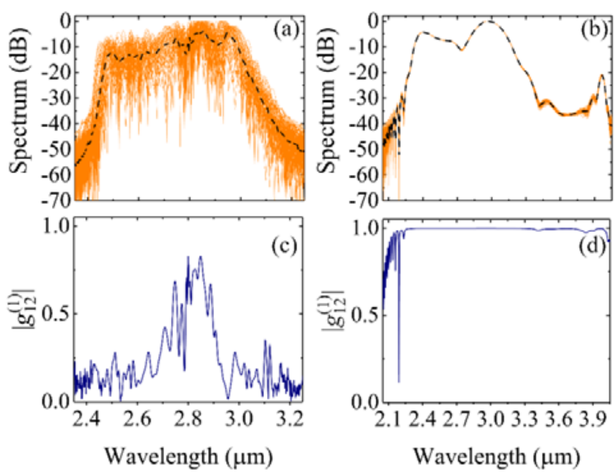

Fig. 12. (a), (b) The spectra and (c), (d) value of first-order coherence $g_{12}^{(1)}$ of the SC generated with the 1 ps and 47.06 fs pulse under noise level $\eta = 0.01$. The orange and black curves in (a) and (b) are the spectra of 50 shots and the average spectra of the 50 shots, respectively.

In order to quantify the improvement of coherence, we vary the strength of random noises and calculate the weighted value of coherence R as [10,51]

$$R = \int_0^\infty \left| g_{12}^{(1)}(\lambda) \right| \bar{P}(\lambda) d\lambda \Big/ \int_0^\infty \bar{P}(\lambda) d\lambda , \tag{10}$$

where $\bar{P}(\lambda) = \left\langle |\tilde{\psi}(\lambda)|^2 \right\rangle$ is the ensemble average of the SC generated with different noise seeds. Fig. 13(a) shows the values of R for 1 ps and 47.06 fs pulses calculated at different η. We use the logarithm scale lg(η) to enlarge the variation of η. From Fig. 13(a), the value of R is approximately equal to 1 when lg(η)<−2 for the 47.06 fs pulse. For the pulse of 1 ps, the value of R is approximately equal to 1 when lg(η)<−4. When −0.3<lg(η)<−3, the change of R for the 47.06 fs pulse is much smaller than that for the 1 ps pulse. In Fig. 13(b), K=lg(1−R) is used for better presentation of the variations of R especially when its value is close to 1. From Fig. 13, lg(η) differs by about 2 for 1 ps and 47.06 fs pulses under the same coherence level. Thus, the noise tolerance is improved about 2 orders of magnitude. Therefore, the self-similar compression can greatly enhance the coherence of the SC generation.

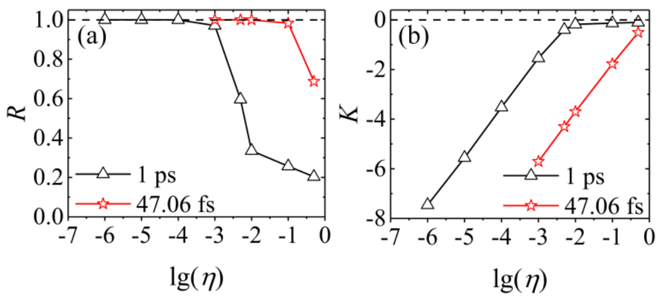

Fig. 13. (a) The weighted value R and (b) K=lg(1−R) as functions of lg(η) for 1 ps (black curves with triangles) and 47.06 fs (red curves with stars) pulse.

6. Conclusion

In summary, we have designed a tapered suspended silicon strip waveguide which has an exponentially decreasing dispersion profile along the direction of propagation for self-similar picosecond pulse compression. In the realistic case with linear and nonlinear losses, variation of $\gamma(z)$, HOD, and HON considered, a 1 ps pulse centred at wavelength 2.8 μm is compressed to 47.06 fs in the 3.9-cm waveguide taper, along with negligible pedestal. The compression factor F_c is 21.25 with a quality factor Q_c of 0.78. We estimate the SC generation with the two pump pulses in a uniform silicon strip waveguide. Simulation results show a significant improvement of the coherence of the generated SC from the compressed pulse comparing to that from picosecond pulse. Such a SC generation scheme with a picosecond input pulse is a promising method to fulfill the on-chip mid-infrared SC source when the mid-infrared mode-locked femtosecond lasers are still lacking.

Acknowledgments

This work was supported in part by the National Natural Science Foundation of China (61875238 and 61475023), Beijing Youth Top-notch Talent Support Program (2015000026833ZK08), Fund of State Key Laboratory of Information Photonics and Optical Communications (BUPT) P. R. China (IPOC2017ZZ05), Shenzhen Science and Technology Innovation Commission (JCYJ20160331141313917), and Research Grant Council of Hong Kong (PolyU152144/15E and PolyU152471/16E).

References

1. B. Jalali, V. Raghunathan, R. Shori, S. Fathpour, D. Dimitropoulps, O. Stafsudd, Prospects for silicon Mid-IR Raman lasers, IEEE J. Sel. Top. Quantum Electron. 12 (2006) 1618-1627.
2. J. Leuthold, C. Koos, W. Freude, Nonlinear silicon photonics, Nat. Photon. 4 (2010) 535-544.
3. M. Nedeljkovic, A. Z. Khokhar, Y. Hu, X. Chen, J. S. Penades, S. Stankovic, H. M. H. Chong, D. J. Thomson, F. Y. Gardes, G. T. Reed, G. Z. Mashanovich, Silicon photonic devices and platforms for the mid-infrared, Opt. Mater. Express 3 (2013) 1205-1214.
4. T. Hu, B. W. Dong, X. S. Luo, T. Y. Liow, J. F. Song, C. K. Lee, G. Q. Lo, Silicon photonic platforms for mid-infrared applications Photon. Res. 5 (2017) 417-430.
5. N. X. Li, E. S. Magden, Z. Su, N. Singh, A. Ruocco, M. Xin, M. Byrd, P. T. Callahan, J. D. B. Bradley, C. Baiocco, D. Vermeulen, M. R. Watts, Broadband 2-µm emission on silicon chips: monolithically Integrated Holmium lasers, Opt. Express 26 (2018) 2220-2230.
6. C. F. Kaminski, R. S. Watt, A. D. Elder, J. H. Frank, J. Hult, Supercontinuum radiation for applications in chemical sensing and microscopy, Appl. Phys. B 92 (2008) 367-378.
7. S. Dupont, C. Petersen, J. Thogersen, C. Agger, O. Bang, S. R. Keiding, IR microscopy utilizing intense supercontinuum light source, Opt. Express 20 (2012) 4887-4892.
8. B. Kuyken, T. Ideguchi, S. Holzner, M. Yan, T. W. Hänsch, J. V. Campenhout, P. Verheyen, S. Coen, F. Leo, R. Baets, G. Roelkens, N. Picqué, An octave-spanning mid-infrared frequency comb generated in a silicon nanophotonic wire waveguide, Nat. Commun. 6 (2015) 6310-1-6.
9. J. M. Dudley, G. Genty, S. Coen, Supercontinuum generation in photonic crystal fiber, Rev. Mod. Phys. 78 (2006) 1135-1184.
10. J. M. Dudley, S. Coen, Coherence properties of supercontinuum spectra generated in photonic crystal and tapered optical fibers, Opt. Lett. 27 (2002) 1180-1182.
11. G. Genty, M. Surakka, J. Turunen, A. T. Friberg, Complete characterization of supercontinuum coherence, J. Opt. Soc. Am. B 28 (2011) 2301-2309.
12. H. Pires, M. Baudisch, D. Sanchez, M. Hemmer, J. Biegert, Ultrashort pulse generation in the mid-IR, Prog. Quantum Electron. 43 (2015) 1-30.
13. F. K. Fatemi, Analysis of nonadiabatically compressed pulses from dispersion-decreasing fiber, Opt. Lett. 27 (2002) 1637-1639.
14. M. L. V. Tse, P. Horak, J. H. V. Price, F. Poletti, F. He, D. J. Richardson, Pulse compression at 1.06 µm in dispersion-decreasing holey fibers, Opt. Lett. 31 (2006) 3504-3506.
15. Q. Li, J. N. Kutz, P. K. A. Wai, Cascaded higher-order soliton for non-adiabatic pulse compression, J. Opt. Soc. Am. B 27 (2010) 2180-2189.
16. R. A. Hussein, M. F. O. Hameed, S. S. A. Obayya, Ultrahigh soliton pulse compression through liquid crystal photonic crystal fiber, IEEE J. Sel. Top. Quantum Electron. 22 (2016) 4900908-1-8.
17. Q. Li, P.K.A. Wai, K. Senthilnathan, K. Nakkeeran, Modeling self-similar optical pulse compression in nonlinear fiber bragg grating using coupled-mode equations, J. Lightwave Technol. 29 (2011) 1293-1305.18. F. Li, Q. Li, J. H. Yuan, P.K.A. Wai, Highly coherent supercontinuum generation with picosecond pulses by using self- similar compression, Opt. Express 22 (2014) 27339-27354.
19. C. Mei, F. Li, J. H. Yuan, Z. Kang, X. T. Zhang, K. R. Wang, X. Z. Sang, Q. Wu, B. B. Yan, X. Zhou, L. Wang, C. X. Yu, P.K.A. Wai, High degree picosecond pulse compression in chalcogenide-silicon slot waveguide taper, J. Lightwave Technol. 34 (2016) 3843-3852.

20. J. H. Yuan, J. Chen, F. Li, C. Mei, Z. Kang, X. T. Zhang, Y. Xu, B. B. Yan, X. Z. Sang, Q. Wu, X. Zhou, K. P. Zhong, K. R. Wang, C. X. Yu, G. Farrell, P.K.A. Wai, Mid-infrared self-similar compression of picosecond pulse in an inversely tapered silicon ridge waveguide, Opt. Express 25 (2017) 33439-33450.
21. Y. Zou, S. Chakravarty, C. J. Chung, X. C. Xu, R. T. Chen, Mid- infrared silicon photonic waveguides and devices, Photon. Res. 6 (2018) 254-276.
22. J. T. Robinson, L. Chen, M. Lipson, On-chip gas detection in silicon optical microcavities, Opt. Express 16 (2008) 4296-4301.
23. S. B. Papp, K. Beha, P. Del'Haye, F. Quinlan, H. Lee, K. J. Vahala, S. A. Diddams, Microresonator frequency comb optical clock, Optica 1 (2014) 10-14.
24. P. Colman, C. Husko, S. Combrié, I. Sagnes, C. W. Wong, A. De Rossi, Temporal solitons and pulse compression in photonic crystal waveguides, Nat. Photon. 4 (2010) 862-868.
25. D. T. H. Tan, P. C. Sun, and Y. Fainman, Monolithic nonlinear pulse compressor on a silicon chip, Nat. Commun. 1 (2010) 116-1-6.
26. R. K. W. Lau, M. R. E. Lamont, A. G. Griffith, Y. Okawachi, M. Lipson, A. L. Gaeta, Octave-spanning mid-infrared supercontinuum generation in silicon nanowaveguides, Opt. Lett. 39 (2014) 4518-4521.
27. N. Singh, D. D. Hudson, Y. Yu, C. Grillet, S. D. Jackson, A. C. Bedoya, A. Read, P. Atanackovic, S. G. Duvall, S. Palomba, B. L. Davies, S. Madden, D. J. Moss, B. J. Eggleton, Midinfrared supercontinuum generation from 2 to 6 μm in a silicon nanowire, Optica 2 (2015) 797-802.
28. G. P. Agrawal, Nonlinear Fiber Optics, fifth ed., Academic, San Francisco, 2013.
29. L. Zhang, A. M. Agarwal, L. C. Kimerling, J. Michel, Nonlinear Group IV photonics based on silicon and germanium: From near- infrared to mid-infrared, Nanophotonics 3 (2014) 247-268.
30. R. Soref, Mid-infrared photonics in silicon and germanium, Nat. Photon. 4 (2010) 495-497.
31. Z. L. Wang, H. J. Liu, N. Huang, Q. B. Sun, J. Wen, X. F. Li, Influence of three-photon absorption on mid-infrared cross-phase modulation in silicon-on-sapphire waveguides, Opt. Express 21 (2013) 1840-1848.
32. V. I. Kruglov, A. C. Peacock, J. D. Harvey, Exact self-similar solutions of the generalized nonlinear Schrödinger equation with distributed coefficients, Phys. Rev. Lett. 90 (2003) 113902-1-4.
33. V. I. Kruglov, A. C. Peacock, J. D. Harvey, Exact solutions of the generalized nonlinear Schrödinger equation with distributed coefficients, Phys. Rev. E 71 (2005) 056619-1-11.
34. R. Loo, G. Wang, L. Souriau, J. C. Lin, S. Takeuchi, G. Brammertz, M. Caymax, High quality Ge virtual substrates on Si wafers with standard STI patterning, J. Electrochem. Soc. 157 (2010) H13-H21.
35. J. Chiles, S. Khan, J. C. Ma, S. Fathpour, High-contrast, all-silicon waveguiding platform for ultra-broadband mid-infrared photonics, Appl. Phys. Lett. 103 (2013) 151106-1-3.
36. D. Y. Oh, K. Y. Yang, C. Fredrick, G. Ycas, S. A. Diddams, K. J. Vahala, Coherent ultra-violet to near-infrared generation in silica ridge waveguides, Nat. Commun. 8 (2017) 13922-1-7.
37. L. Zhang, Y. Yue, R. G. Beausoleil, A. E. Willner, Flattened dispersion in silicon slot waveguides, Opt. Express 18 (2010) 20529-20534.
38. P. K. A. Wai, H. H. Chen, Y. C. Lee, Radiations by "solitons" at the zero group-dispersion wavelength of single-mode optical fibers, Phys. Rev. A 41 (1990) 426-439.
39. G. P. Agrawal, Nonlinear Fiber Optics, second ed., Academic, San Francisco, 2009.
40. G. L. Li, J. Yao, Y. Luo, H. Thacker, A. Mekis, X. Z. Zheng, I. Shubin, J. H. Lee, K. Raj, J. E. Cunningham, A. V. Krishnamoorthy, Ultralow-loss, high-density SOI optical waveguide routing for macrochip interconnects, Opt. Express 20 (2012) 12035-12039.
41. S. Pearl, N. Rotenberg N, H. M. V. Driel, Three photon absorption in silicon for 2300–3300nm, Appl. Phys. Lett. 93 (2008) 131102-1-3.
42. K. Senthilnathan, Q. Li, K. Nakkeeran, P. K. A. Wai, Robust pedestal-free pulse compression in cubic-quintic nonlinear media, Phys. Rev. A 78 (2008) 033835-1-12.
43. T. Aalto, K. Solehmainen, M. Harjanne, M. Kapulainen, P. Heimala, Low-loss converters between optical silicon waveguides of different sizes and types, IEEE Photonics Technol. Lett. 18 (2006) 709-711.
44. R. Dangel, A. L. Porta, D. Jubin, F. Horst, N. Meier, M. Seifried, B. J. Offrein, Polymer waveguides enabling scalable low- loss adiabatic optical coupling for silicon photonics, IEEE J. Sel. Top. Quantum Electron 24 (2018) 8200211-1-11.
45. J. M. Dudley, S. Coen, Numerical simulations and coherence properties of supercontinuum generation in photonic crystal and tapered optical fibers, IEEE J. Sel. Top. Quantum Electron. 8 (2002) 651-659.
46. G. Genty, M. Lehtonen, H. Ludvigsen, Enhanced bandwidth of supercontinuum generated in microstructured fibers, Opt. Express 12 (2004) 3471-3480.
47. K. R. Khan, M. F. Mahmood, A. Biswas, Coherent supercontinuum generation in photonic crystal fibers at visible and near infrared wavelengths, IEEE J. Sel. Top. Quantum Electron. 20 (2014) 7500309-1-9.
48. U. D. Dave, C. Ciret, S. P. Gorza, S. Combrie, A. D. Rossi, F. Raineri, G. Roelkens, and B. Kuyken, Dispersive-wave-based octave-spanning supercontinuum generation in InGaP membrane waveguides on a silicon substrate, Opt. Lett. 40 (2015) 3584-3587.
49. L. Zhang, Q. Lin, Y. Yue, Y. Yan, R. G. Beausoleil, A. Agarwal, L. C. Kimerling, J. Michel, A. E. Willner, On-chip octave-spanning supercontinuum in nanostructured silicon waveguides using ultralow pulse energy, IEEE J. Sel. Top. Quantum Electron. 18 (2012) 1799-1806.
50. R. R. Fan, C. L. Wu, Y.Y. Lin, C. Y. Liu, P. S. Hwang, C. W. Liu, J. P. Qiao, M. H. Shih, Y. J. Hung, Y. J. Chiu, A. K. Chu, C. K. Lee , Visible to near-infrared octave spanning supercontinuum generation in tantalum pentoxide (Ta_2O_5) air-cladding waveguide, Opt. Lett. 44 (2019) 1512-1515.
51. J. H. Yuan, Z. Kang, F. Li, X. T. Zhang, X. Z. Sang, Q. Wu, B. B. Yan, K. R. Wang, X. Zhou, K. P. Zhong, G. Y. Zhou, C. X. Yu, C. Lu, H. Y. Tam, P.K.A. Wai, Mid-infrared octave-spanning supercontinuum and frequency comb generation in a suspended germanium-membrane ridge waveguide, J. Lightwave Technol. 35 (2017) 2994-3002.